



# Microstructural Evaluation and Highly Efficient Photocatalytic Degradation Characteristic of Nanostructured $\text{Mg}_{65}\text{Ni}_{20}\text{Y}_{15-x}\text{La}_x$ ( $X = 1, 2, 3$ ) Alloys

Celal Kursun<sup>1,2</sup> · Musa Gogebakan<sup>2</sup> · Hasan Eskalen<sup>3</sup> · Serhan Uruş<sup>4</sup> · John H. Perepezko<sup>1</sup>

Received: 3 December 2018 / Accepted: 29 May 2019 / Published online: 1 June 2019  
© Springer Science+Business Media, LLC, part of Springer Nature 2019

## Abstract

A series of La and Y rates of  $\text{Mg}_{65}\text{Ni}_{20}\text{Y}_{15-x}\text{La}_x$  ( $X = 1, 2, 3$ ) alloys was synthesized by mechanical alloying in order to investigate the influence of varying amounts of Y and La on the microstructure and degradation performance of methyl blue. The nano-structured alloys were characterized by X-ray diffraction, scanning electron microscopy, energy dispersive spectrometry (EDX), UV–Vis spectroscopy (UV) and Fourier-Transform Infrared Spectroscopy (FTIR) techniques. Three different intermetallic phases such as  $\text{Mg}_{24}\text{Y}_5$ ,  $\text{Mg}_{17}\text{La}_2$  and  $\text{Mg}_2\text{Ni}$  were obtained after 75 h of milling time. With an increase in the milling time, the particle and crystallite size of the  $\text{Mg}_{65}\text{Ni}_{20}\text{Y}_{15-x}\text{La}_x$  ( $X = 1, 2, 3$ ) powders were decreased and the crystallite sizes of the alloys were calculated below 20 nm after 75 h of milling time. The composition of the nanostructured powders after mechanical alloying were determined to be very close to the initial composition by EDX analyses. The time and amount-dependent photocatalytic degradation of methyl blue samples were investigated under visible light at room temperature. The photocatalytic degradation properties of methyl blue in the water samples were evaluated by recording the decrease of absorbances at 590 nm in UV–Vis absorption spectra. The nanostructured  $\text{Mg}_{65}\text{Ni}_{20}\text{Y}_{15-x}\text{La}_x$  ( $X = 1, 2, 3$ ) powders demonstrated highly efficient photocatalytic properties in daylight even in the absence of any oxidant, heat or light source. After a 30 min exposure, the UV–Vis and FT-IR spectra indicated that the methyl blue samples became colourless using  $\text{Mg}_{65}\text{Ni}_{20}\text{Y}_{15-x}\text{La}_x$  ( $X = 1, 2, 3$ ) type catalysts. Among the alloys, the  $\text{Mg}_{65}\text{Ni}_{20}\text{Y}_{13}\text{La}_2$  is the best catalyst for the photocatalytic degradation of methyl blue possibly because of it had the smallest crystalline size compared to the other alloys.

**Keywords** Nanocrystalline powders · Mg based alloys · Mechanical alloying · Methyl blue · Degradation · Dye

## 1 Introduction

The first commercial synthetic dye was discovered by Henry Perkin in 1856 [1] and from this initial discovery, the need for synthetic dyes has increased continuously. Today, more than 100,000 different structured dyes have been synthesized [2] and over 10 million metric tons synthetic dyes are produced with a 3–4% growth rate [3]. Unfortunately, these synthetic dyes are the main cause of wastewater and the effluents pollute not only water but also the land [4]. Moreover, some of them can also have mutagenic, genotoxic and carcinogenic effects for human and animals [5].

Amorphous and nanocrystalline materials are known as functional materials with superior properties [6–16]. Recently, the use of nanostructured and amorphous materials in the treatment of wastewater has attracted considerable attention [17]. Among the variety of different metallic glasses, Fe-based and Mg-based alloys have received

✉ Celal Kursun  
ckursun@wisc.edu; celalkursun@hotmail.com

<sup>1</sup> Department of Materials Science and Engineering,  
University of Wisconsin – Madison, Madison, WI 53706,  
USA

<sup>2</sup> Department of Physics, Faculty of Art and Sciences,  
Kahramanmaraş Sutcu Imam University,  
46100 Kahramanmaraş, Turkey

<sup>3</sup> Department of Materials Sciences and Engineering,  
Kahramanmaraş Sutcu Imam University,  
46100 Kahramanmaraş, Turkey

<sup>4</sup> Department of Chemistry, Faculty of Art  
and Sciences, Kahramanmaraş Sutcu Imam University,  
46100 Kahramanmaraş, Turkey

the most attention. For example, Wang et al. examined  $\text{Fe}_{78}\text{Si}_9\text{B}_{13}$  alloys for rhodamine B dye removal [18]. The degradation capacities of Fe-based amorphous alloys, other than  $\text{Fe}_{78}\text{Si}_9\text{B}_{13}$  for different types and dye structures have been examined extensively [19–27]. However, the study of Mg–Zn based alloys revealed that Mg based alloys exhibit a degradation capacity that is higher than that for the Fe based powders [28].

Although there are studies about Mg–Ni–Y based alloys [29–33], the degradation performance of these alloys with the addition of La has not been examined previously. Moreover, the photocatalytic degradation performances of these alloys have not been examined for methyl blue. Therefore, the aim of this work is to produce Mg based quaternary alloys with systematically increasing the La level by the mechanical alloying technique. Then, the effect of increasing amount of La on the microstructure of Mg–Ni–Y alloy system and on the degradation of methyl blue was examined under different conditions.

## 2 Methods and Materials

### 2.1 Alloy Production

Pure Mg (99.9%), Ni (99.7%), Y (99.8%) and La (99.9%) elemental powders were mechanically alloyed in planetary-ball mill (Fritsch Pulverisette 5). These elemental powders were accurately weighted in a glove box under an argon atmosphere. The mechanical alloying was performed in room temperature under an argon atmosphere at a speed of 300 rpm and a small amount of powder was taken at selected times (5 h, 25, 50 h and 75 h) for additional characterization. The mechanical alloying (MA) conditions are given at Table 1.

The structural evolution and the phase identification of the alloys were determined X-ray diffraction (XRD) with  $\text{CuK}_\alpha$  radiation ( $\lambda = 0.154$  nm) at 40 kV and 30 mA. The surface morphology and composition of the powder particles were characterized by scanning electron microscopy (SEM)

with a JEOL JCM 5000 scanning electron microscope at an acceleration voltage of 10 kV with an energy-dispersive X-ray spectrometer (EDX).

### 2.2 Dye Degradation

Methyl Blue samples in water were used as dye samples in the photocatalytic degradation experiments. The degradation efficiencies of the nanostructured-alloys were evaluated by using UV–Vis spectroscopy (Shimadzu-1800) during the photocatalytic degradation reaction. First, a control sample was scanned in the range of 200–800 nm at 1 nm intervals. The maximum absorption peak was determined as 590 nm for the methyl blue samples in water. The spectra of the water samples during the degradation process were recorded between 400 and 800 nm at 1 nm intervals. The absorbances were collected at 590 nm for each water samples. The concentration of methyl blue dye samples was 100 ppm (mg/L) for each degradation test. Different amounts of nanostructured-alloys (0.025 g, 0.05 g and 0.1 g) were added to each dye samples in water and stirred for 90 min. at room temperature. The samples were collected at times of 5, 10, 15, 20, 30, 40 and 60 min., filtered and scanned in UV–Vis spectrophotometer during the photocatalytic degradation reaction. In addition, time-dependent degradation properties of the nanostructured-alloys were investigated in the kinetic mode in the instrument.

## 3 Results and Discussion

### 3.1 Microstructural Evaluation

XRD patterns of  $\text{Mg}_{65}\text{Ni}_{20}\text{Y}_{15-x}\text{La}_x$  ( $X = 1, 2, 3$ ) alloys obtained at different milling times are shown in Fig. 1. After 5 h of milling, the XRD patterns exhibited initial crystalline peaks, corresponding to elemental Mg, Ni, La and Y (Fig. 1a–c). By increasing the milling time to 25 h, the intensities of the initial crystalline peaks decreased and the peaks became broader. The broadening is mainly due to the increase in the internal lattice strain and the refinement of the crystal size. However, after 50 h of milling, the elemental peaks disappeared, and new broad peaks developed as clearly seen in Fig. 1a–c. The absence of elemental diffraction peaks suggests the dissolution of elements with the start of the alloying process. Therefore, the observed new peaks were identified as the  $\text{Mg}_{24}\text{Y}_5$ ,  $\text{Mg}_{17}\text{La}_2$  and  $\text{Mg}_2\text{Ni}$  intermetallic phases. The rate of dissolution of La in the alloy is low, and probably associated with the limited solid solubility of La in Mg, Ni and Y. On the other hand, the further increase of milling time up to 75 h, no significant change has been observed in the XRD patterns for the  $\text{Mg}_{65}\text{Ni}_{20}\text{Y}_{15-x}\text{La}_x$  ( $X = 1, 2, 3$ ) alloys.

**Table 1** The operating conditions of mechanical alloying

Rotation speed (rpm)	300
Cup structure	Stainless steel
Cup capacity (ml)	250
Ball structure	Stainless steel
Ball diameter (mm)	8
Ball to mass powder ratio	20:1
Process control agents	1 wt% stearic acid
Atmosphere	Argon
MA time (h)	0–75

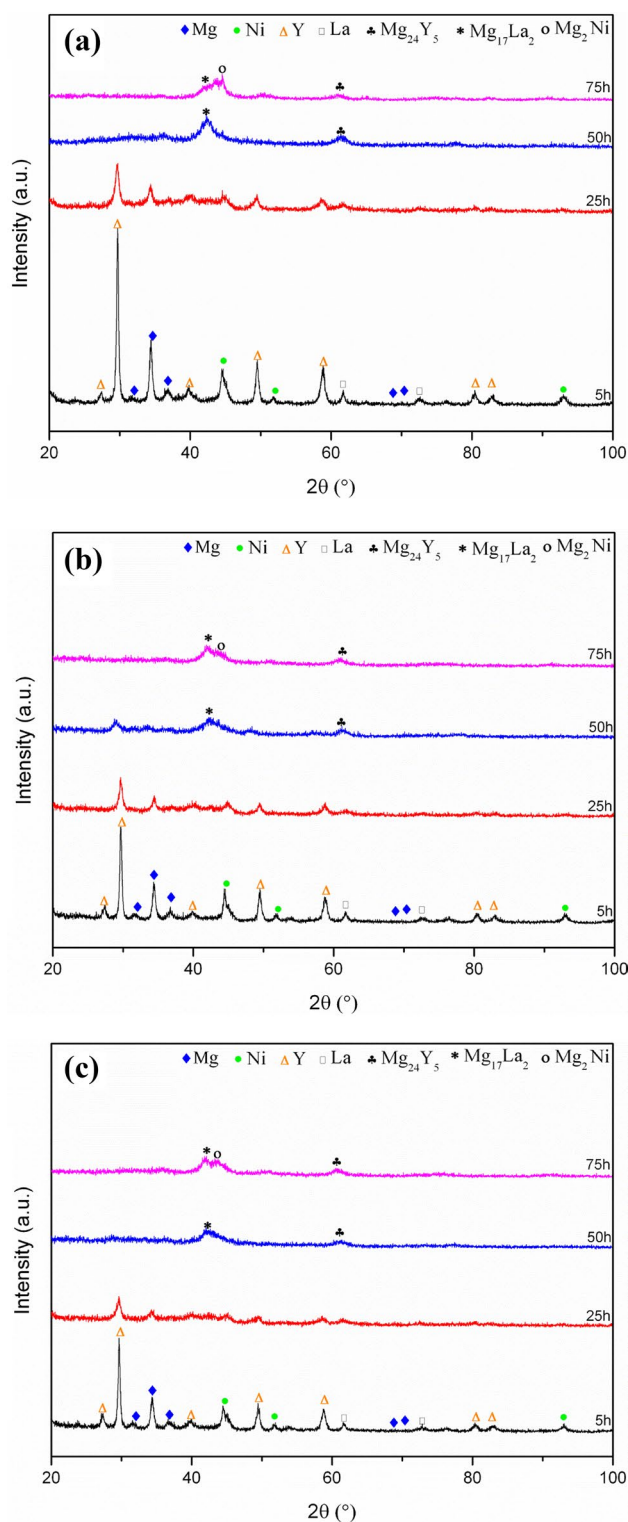


**Fig. 1** XRD patterns of the mechanically alloyed powders after different milling time intervals: **a**  $\text{Mg}_{65}\text{Ni}_{20}\text{Y}_{14}\text{La}_1$ , **b**  $\text{Mg}_{65}\text{Ni}_{20}\text{Y}_{13}\text{La}_2$ , **c**  $\text{Mg}_{65}\text{Ni}_{20}\text{Y}_{12}\text{La}_3$

In order to study the microstructural evolutions during mechanical alloying, the milled powders were also investigated by using SEM. SEM micrographs for  $\text{Mg}_{65}\text{Ni}_{20}\text{Y}_{15-x}\text{La}_x$  ( $X = 1, 2, 3$ ) powders as-received and after various mechanical milling times are shown in Fig. 2. As seen in Fig. 2a, the as-received powders had different size distributions and shapes. After 5 h of milling, the change of the particle size and shapes was not significant. In this case the particle sizes range from about 10  $\mu\text{m}$  to 50  $\mu\text{m}$ . However, after further milling up to 25 h, the average particle size decreases and the cold welding induced by the colliding balls leads to the formation of rather large agglomerates. This is due to the high energy transferred to the powder particles after 25 h of milling. After further milling up to 50 h, the powders exhibit a high degree of agglomeration as can be seen in the SEM micrograph. Because of the repeated fracturing and cold-welding processes, the particles sizes of the fine powders decrease below 10  $\mu\text{m}$  in the mechanical alloying process. As seen in Fig. 2e, the agglomerated powder particles remain as the typical dominant structure, especially after 75 h of milling and the particle sizes decrease to approximately 2  $\mu\text{m}$ .

The homogeneity of the metastable materials is a significant parameter in influencing their performance. As an example, the produced nanostructured  $\text{Mg}_{65}\text{Ni}_{20}\text{Y}_{14}\text{La}_1$  alloy was investigated by EDX to determine the compositional homogeneity. In Fig. 3, the EDX analysis of the  $\text{Mg}_{65}\text{Ni}_{20}\text{Y}_{14}\text{La}_1$  powders is shown after 75 h of milling time. It can be seen clearly in Fig. 3, that the Mg, Ni, Y and La elements are present the  $\text{Mg}_{65}\text{Ni}_{20}\text{Y}_{14}\text{La}_1$  powder alloy. Moreover, the composition of the  $\text{Mg}_{65}\text{Ni}_{20}\text{Y}_{14}\text{La}_1$  alloy is close to the initially intended composition value. This result reveals that all elements of the powder alloy were incorporated without significant loss during mechanical alloying.

The crystallite size of the materials affects their microstructures and their performance for applications. The crystalline sizes of  $\text{Mg}_{65}\text{Ni}_{20}\text{Y}_{15-x}\text{La}_x$  ( $X = 1, 2, 3$ ) alloys were determined by the Debye–Scherrer analysis to understand the effect on the microstructural changes and degradation performance [34–36]. Equation (1) was used to calculate the crystallite sizes of the Mg-based powders.

$$D = \frac{0.9\lambda}{B \cos \theta} \quad (1)$$

where  $D$  is the average crystallite size,  $\lambda$  the X-ray wavelength,  $B$  the full width (in radians) at half maximum intensity and  $\theta$  the Bragg diffraction angle.

Figure 4 shows the variation of crystallite sizes of the  $\text{Mg}_{65}\text{Ni}_{20}\text{Y}_{15-x}\text{La}_x$  ( $X = 1, 2, 3$ ) alloys at different mechanical alloying times. As shown in Fig. 4, the crystallite sizes of  $\text{Mg}_{65}\text{Ni}_{20}\text{Y}_{15-x}\text{La}_x$  ( $X = 1, 2, 3$ ) powders clearly decrease and are calculated 20.9 nm, 15.6 nm and 17.9 nm, respectively, after 25 h of milling time. After 50 h milling time,

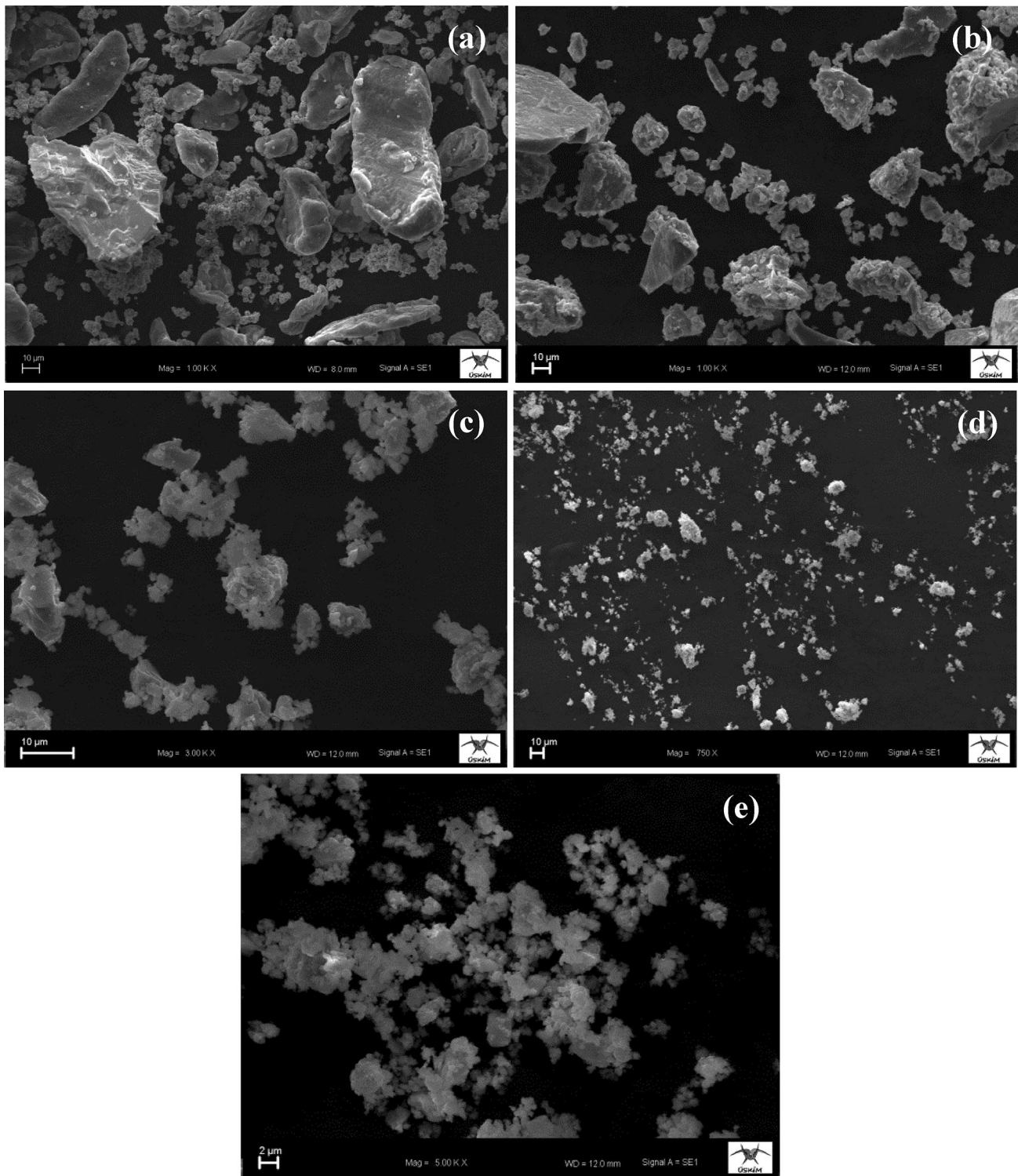


**Fig. 2** Morphological changes of the  $\text{Mg}_{65}\text{Ni}_{20}\text{Y}_{14}\text{La}_1$  powders as a function of the milling time: **a** 0 h; **b** 5 h; **c** 25 h; **d** 50 h; **e** 75 h

the crystallite sizes of the Mg-based alloys are determined as 18.8 nm for  $\text{Mg}_{65}\text{Ni}_{20}\text{Y}_{14}\text{La}_1$ , 10.8 nm for  $\text{Mg}_{65}\text{Ni}_{20}\text{Y}_{13}\text{La}_2$  and 15.4 nm for  $\text{Mg}_{65}\text{Ni}_{20}\text{Y}_{12}\text{La}_3$ . The average crystallite sizes of  $\text{Mg}_{65}\text{Ni}_{20}\text{Y}_{15-x}\text{La}_x$  ( $X=1, 2, 3$ ) alloys reach the

lowest values. These values for  $\text{Mg}_{65}\text{Ni}_{20}\text{Y}_{15-x}\text{La}_x$  ( $X=1, 2, 3$ ) powders are calculated as 18.2 nm, 6.8 nm and 10.9 nm, respectively, after 75 h of milling. These values are also listed Table 2.

**Fig. 3** Typical EDX analysis result of the mechanically alloyed  $\text{Mg}_{65}\text{Ni}_{20}\text{Y}_{14}\text{La}_1$  powders

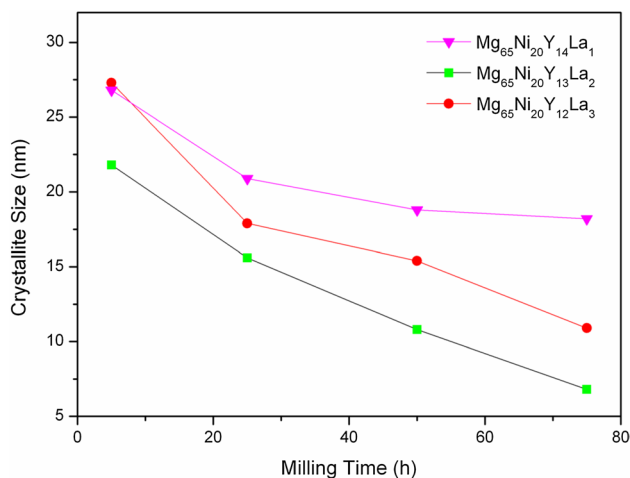
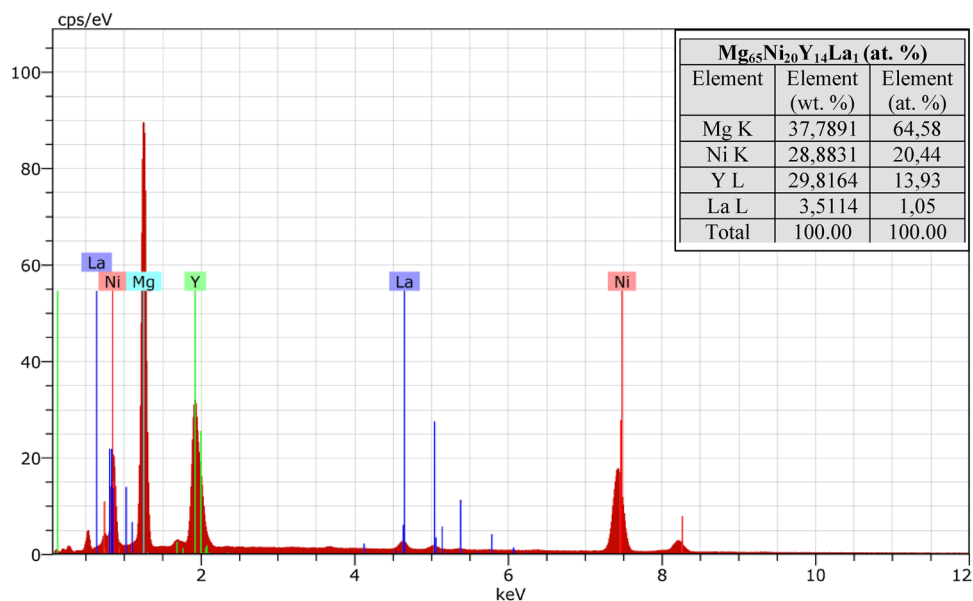


**Fig. 4** Crystal size of mechanically alloyed  $\text{Mg}_{65}\text{Ni}_{20}\text{Y}_{15-x}\text{La}_x$  ( $X=1, 2, 3$ ) powders as a function of milling time

### 3.2 Photocatalytic Degradation of Methyl Blue Using Nanostructured-Alloys of methyl blue can be examined

The time and amount-dependent photocatalytic degradation of methyl blue were investigated under daylight at room temperature. Different amounts of the  $\text{Mg}_{65}\text{Ni}_{20}\text{Y}_{15-x}\text{La}_x$  ( $X=1, 2, 3$ ) nanostructured-alloys (0.025 g, 0.05 g and 0.1 g) were added to methyl blue samples in water (100 mg/L) and stirred for 90 min. The samples were collected and filtered at 5, 10, 15, 20, 30, 40 and 60 min for each trial. The filtered water samples were scanned in UV–Vis spectrophotometer in the range of 400–800 nm. The degradations of methyl

**Table 2** Crystallite sizes of mechanically alloyed  $\text{Mg}_{65}\text{Ni}_{20}\text{Y}_{15-x}\text{La}_x$  ( $X=1, 2, 3$ ) powders as a function of milling time

MA time (h)	Crystallite size (nm)		
	$\text{Mg}_{65}\text{Ni}_{20}\text{Y}_{14}\text{La}_1$	$\text{Mg}_{65}\text{Ni}_{20}\text{Y}_{13}\text{La}_2$	$\text{Mg}_{65}\text{Ni}_{20}\text{Y}_{12}\text{La}_3$
5	26.8	21.8	27.3
25	20.9	15.6	17.9
50	18.8	10.8	15.4
75	18.2	6.8	10.9

blue in the water samples were determined by recording the decrease of absorbance at 590 nm in UV–Vis absorption spectra.

When the FT-IR spectra of the samples were evaluated after the photocatalytic degradation tests, it is possible to mention that the dissolved methyl blue dye in water was completely degraded (Fig. 5). After the degradation process, the aromatic C–H stretches observed about  $3050\text{ cm}^{-1}$  and the secondary amine N–H stretches seen around  $3249\text{ cm}^{-1}$  were removed in FT-IR spectrum. Additionally, the stretches of the functional groups of methyl blue, such as, aromatic C=C stretches around  $1568\text{ cm}^{-1}$ , the aromatic C–N stretches around  $1000\text{--}1160\text{ cm}^{-1}$  and the S=O stretch at  $1331\text{ cm}^{-1}$  were not observed in the FT-IR spectra after the degradation tests. However,  $\text{CO}_2$  formation was observed after the degradation in the of FT-IR spectrum. Asymmetric vibrations appeared strongly at  $2350\text{ cm}^{-1}$  and  $2390\text{ cm}^{-1}$  whereas bending modes were seen at around  $580\text{ cm}^{-1}$  with a broad band. Multiple peaks around  $1900\text{--}2200\text{ cm}^{-1}$  were possibly the stretches of the substituents in the degradation

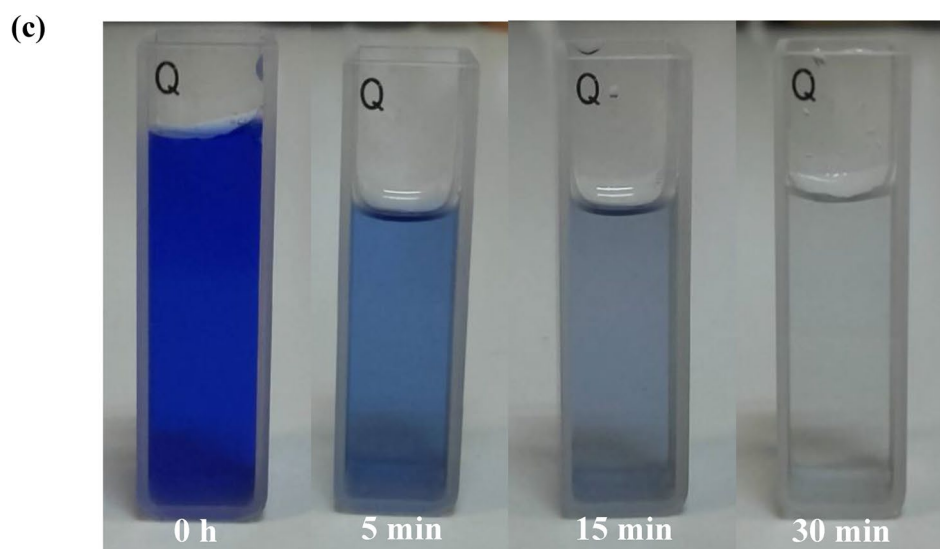
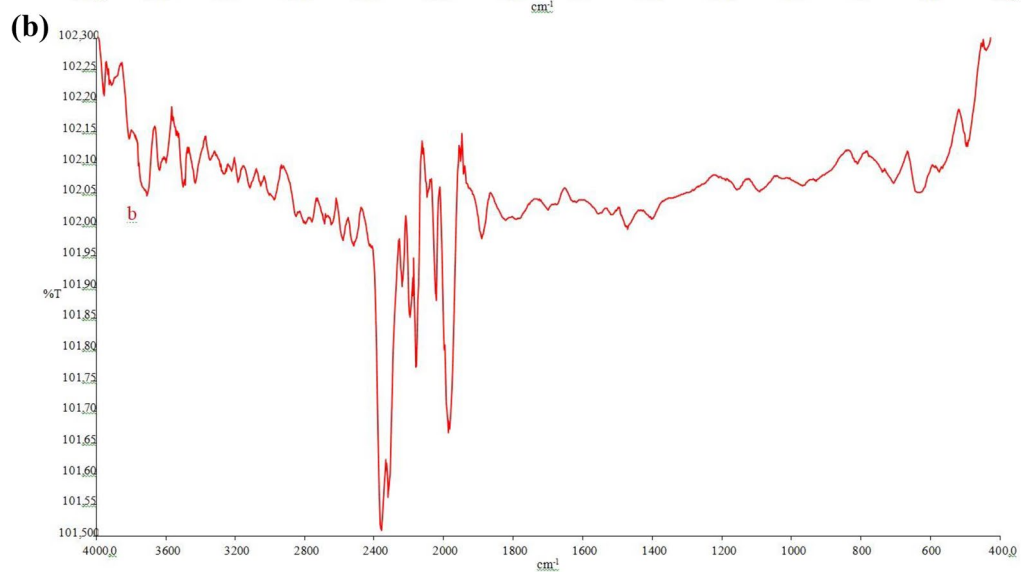
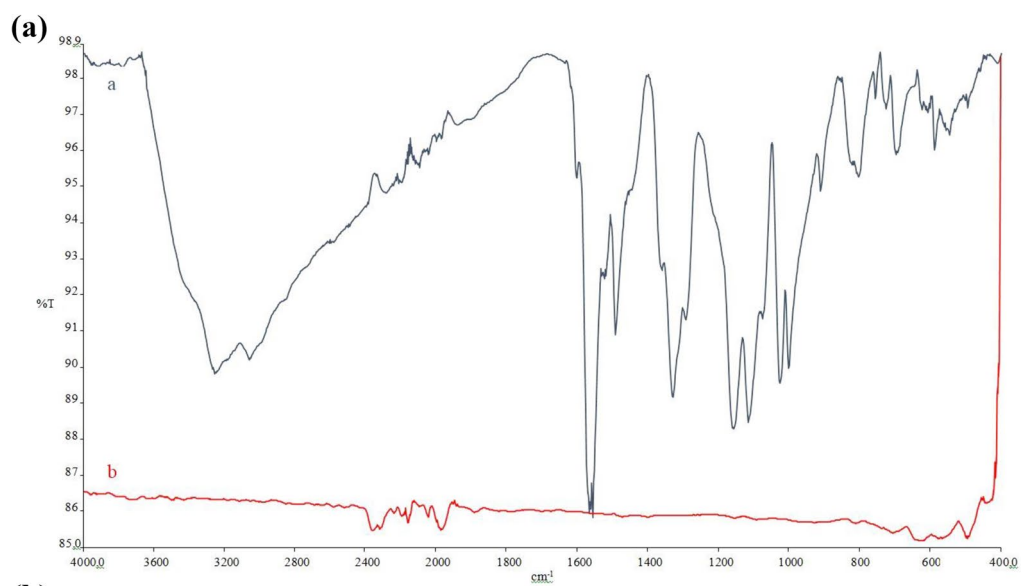


**Fig. 5** FT-IR spectra **a** methyl blue, **b** after photocatalytic reaction, **c** the colour change as a function of degradation time for  $\text{Mg}_{65}\text{Ni}_{20}\text{Y}_{13}\text{La}_2$  alloy (Color figure online)

products such as  $\text{O}-\text{C}\equiv\text{N}$  (cyanate),  $\text{N}=\text{C}=\text{O}$  (isocyanate),  $\text{S}-\text{C}\equiv\text{N}$  (thiocyanate) and  $\text{N}=\text{C}=\text{S}$  (thiocyanate) structures. Moreover, weak sulphate  $\text{S}=\text{O}$  stretches were observed at  $1100\text{ cm}^{-1}$  and  $620\text{ cm}^{-1}$ .

Finally, the whole of the reaction medium turned colourless after approximately in 30 min for all the tests using

$\text{Mg}_{65}\text{Ni}_{20}\text{Y}_{15-x}\text{La}_x$  ( $X=1, 2, 3$ ) alloys as observed both in the UV–Vis and the FT-IR spectra of the samples. Because of the smaller crystalline size,  $\text{Mg}_{65}\text{Ni}_{20}\text{Y}_{13}\text{La}_2$  has been showed the best photo-catalytic activities compared to the other nanostructured-alloys (Figs. 5, 6). Figure 5c shows the colour change taking place from dark blue to colourless as a function of degradation time for the  $\text{Mg}_{65}\text{Ni}_{20}\text{Y}_{13}\text{La}_2$  alloy. In addition to the FT-IR spectra, the UV–Vis absorbance spectra also shows the degradation of methyl blue in the range of 400–800 nm in Figs. 6 and 7. According to the

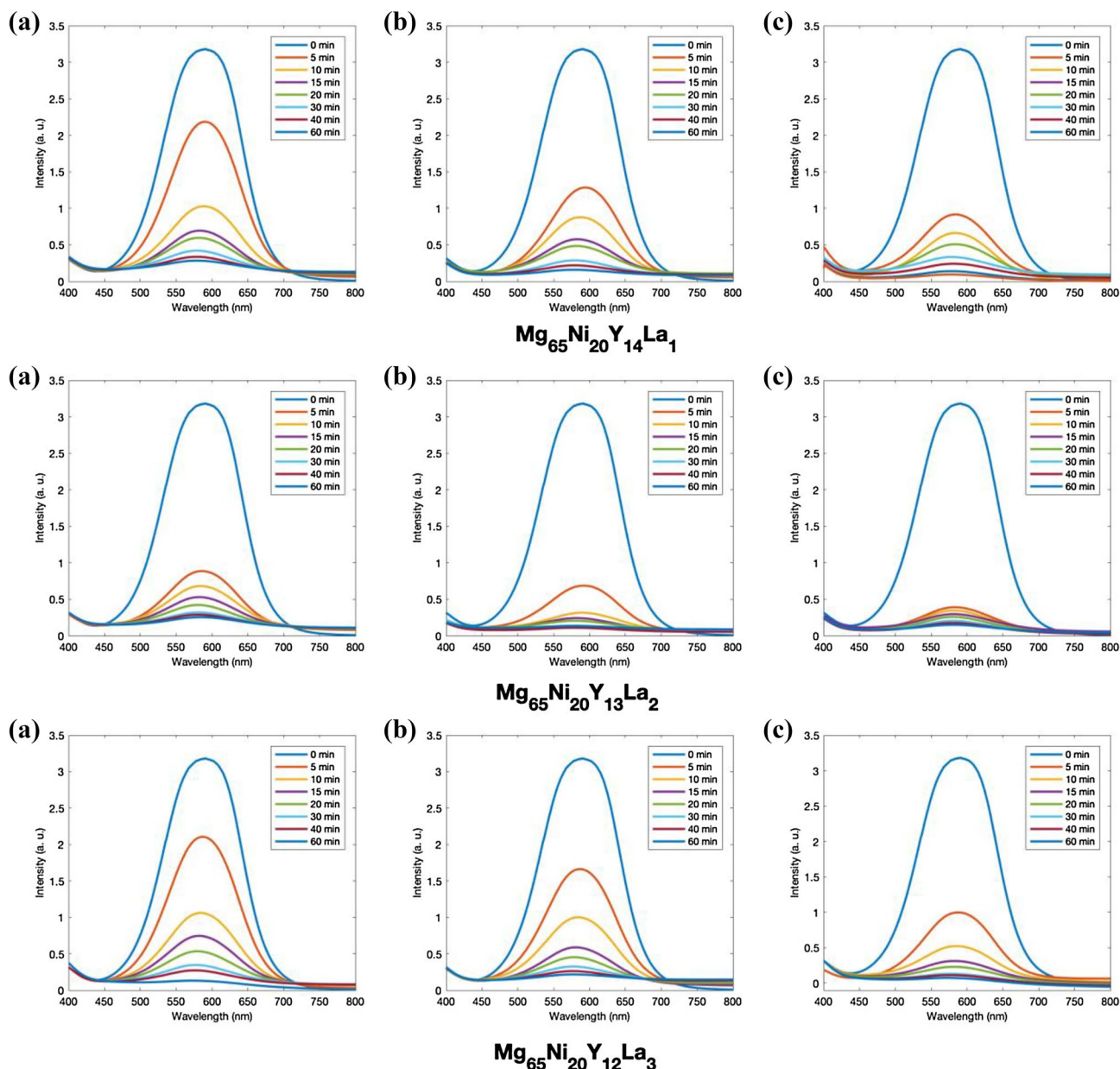


**Fig. 6** UV–Vis spectra of time dependent photocatalytic degradation of mechanically alloyed  $\text{Mg}_{65}\text{Ni}_{20}\text{Y}_{15-x}\text{La}_x$  ( $X=1, 2, 3$ ) alloys. **a** 0.25 mg catalyst/mL dye solution, **b** 0.50 mg catalyst/mL dye

solution, **c** 1.0 mg catalyst/mL dye solution. (Dye concentration: 100 mg/L) (Color figure online)

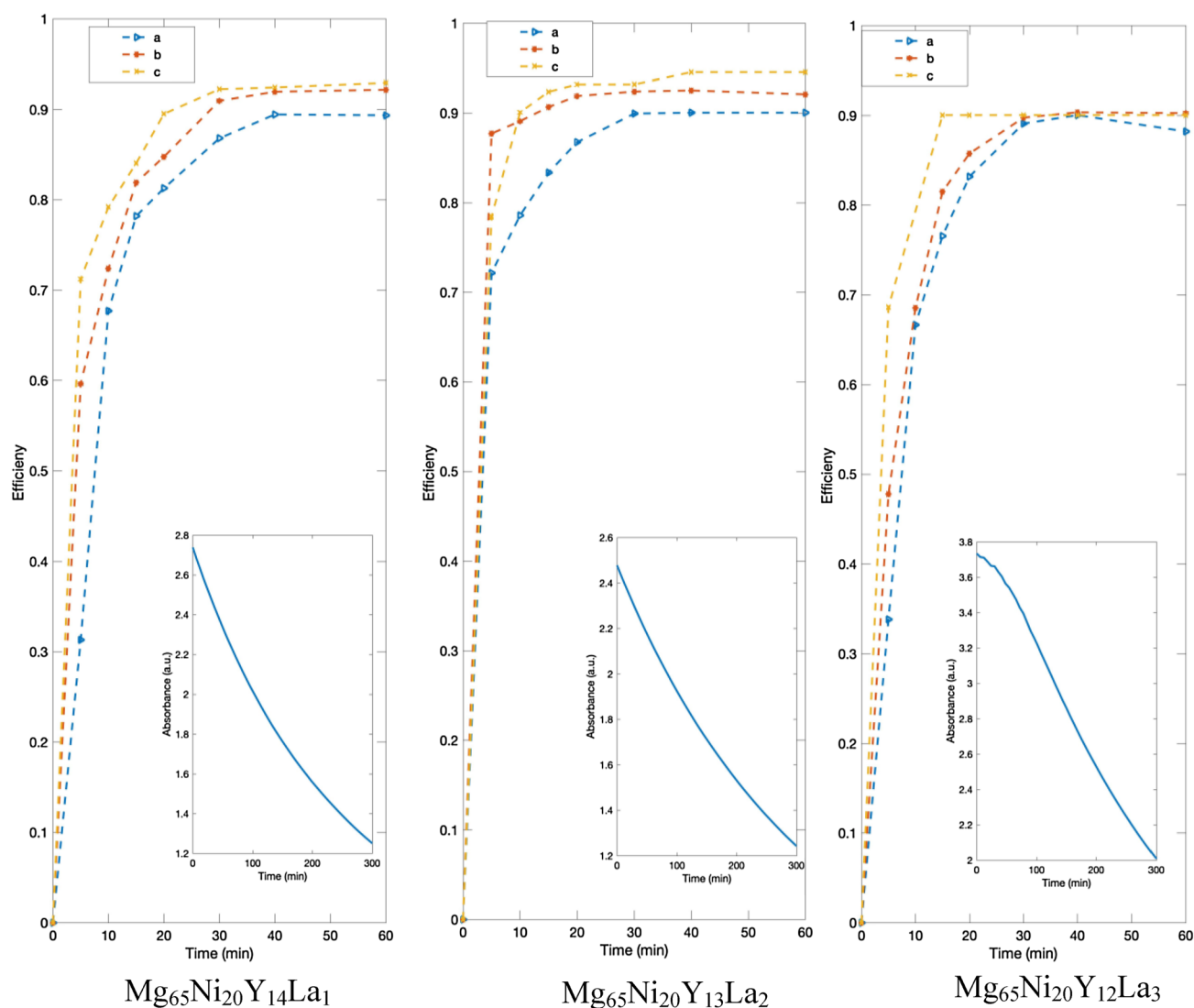


**Fig. 7** Photocatalytic degradation efficiency of mechanically alloyed  $\text{Mg}_{65}\text{Ni}_{20}\text{Y}_{15-x}\text{La}_x$  ( $X = 1, 2, 3$ ) powders; (a) 0.25 mg catalyst/mL dye solution, (b) 0.50 mg catalyst/mL dye solution, (c) 1.0 mg catalyst/mL dye solution

probable mechanism of the heterogeneous photocatalytic degradation of methyl blue under visible light irradiation, firstly, the electrons in the valence band in the alloy crystal can be excited to the conduction band and the positive holes are left in the conduction band on the surface of the nanostructured-alloy. Photo-generated electrons in conduction band react with acceptors and form a radical anion  $\text{O}_2^{\cdot-}$ . In addition, the mechanically alloyed  $\text{Mg}_{65}\text{Ni}_{20}\text{Y}_{15-x}\text{La}_x$  ( $X = 1, 2, 3$ ) powders receive an electron for positive holes from water and produced  $\text{OH}^{\cdot}$  radicals. During this process, methyl blue having negative sulfonate groups electrostatically attracts to the positively charged surface of the alloy. Finally, the dye is oxidized by the radical moieties to carbon dioxide and water [37–40]. The mechanism mentioned above is schematically illustrated in Fig. 8.

According to the degradation efficiency (Fig. 7), the photocatalytic degradation of methyl blue was essentially completed in 20 min. Thus, the plot of  $\ln(C_t/C_0)$  versus time for photocatalytic degradation of methyl blue can be examined by

$$\ln(C_t/C_0) = -k \cdot t \quad (2)$$

where  $k$  is the photo-degradation rate constant ( $\text{min}^{-1}$ ) and  $C_0$  and  $C_t$  are the concentrations (mg/L) of methyl blue at different photocatalytic degradation times, respectively. The linear fit between  $\ln(C_t/C_0)$  and reaction time for different  $\text{Mg}_{65}\text{Ni}_{20}\text{Y}_{15-x}\text{La}_x$  ( $X = 1, 2, 3$ ) alloy catalyses (Fig. 9) follows a pseudo-first-order kinetics behaviour [36, 37]. The photocatalytic degradation kinetics of methyl blue was found as pseudo first order with the determination coefficients of



**Fig. 8** Possible photocatalytic degradation mechanism

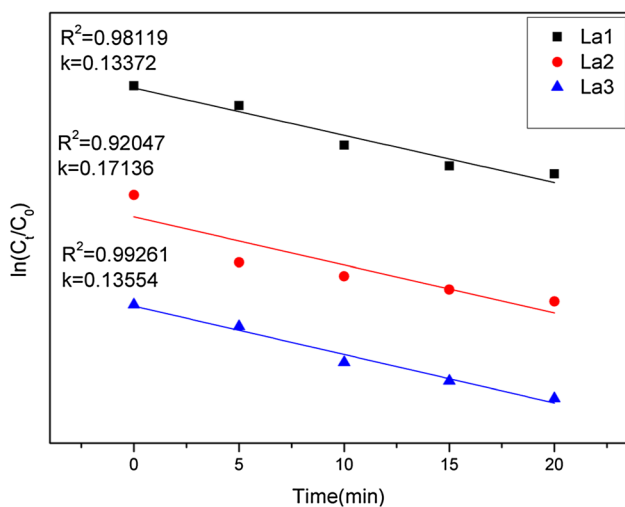
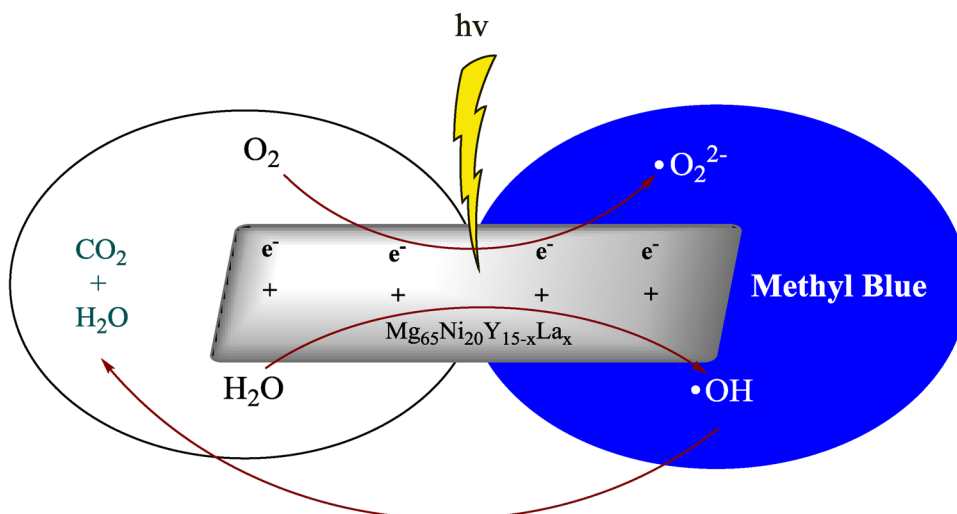


**Fig. 9** Photocatalytic degradation kinetic curves of methyl blue

0.9812, 0.9205 and 0.9926 by  $Mg_{65}Ni_{20}Y_{15-x}La_x$  ( $X = 1, 2, 3$ ), respectively (Fig. 9).

## 4 Conclusions

In the present study, the influence of La addition in the Mg–Ni–Y alloys during mechanical alloying on the microstructural evolutions and the degradation effect on the absorption features of Methyl Blue were characterised and the following results were obtained.

1. Nanocrystalline  $Mg_{65}Ni_{20}Y_{15-x}La_x$  ( $X = 1, 2, 3$ ) powders were successfully manufactured by mechanical alloying.

$Mg_{24}Y_5$ ,  $Mg_{17}La_2$  and  $Mg_2Ni$  phases were obtained after 75 h milling time.

2. The composition of the nanostructured  $Mg_{65}Ni_{20}Y_{14}La_1$  powders were determined very close to initial composition values.
3. The crystallite sizes of the  $Mg_{65}Ni_{20}Y_{15-x}La_x$  ( $X = 1, 2, 3$ ) powders decreased with increasing milling time and the calculated values were 18.2 nm, 6.8 nm and 10.9 nm after 75 h of milling time.
4. Nanostructured  $Mg_{65}Ni_{20}Y_{15-x}La_x$  ( $X = 1, 2, 3$ ) powders showed very efficient photocatalytic properties for methyl blue degradation in daylight without using any oxidant, heat or light source.

**Acknowledgements** The authors thank TÜBİTAK for financial support of the research programme (Project No:114M457). We also thank Kahramanmaraş Sütçü İmam University (Project No: 2017/1-82 M) for financial supports.

## References

1. D. Wesenberg, I. Kyriakides, S.N. Agathos, White-rot fungi and their enzymes for the treatment of industrial dye effluents. *Biotechnol. Adv.* **22**(1–2), 161–187 (2003)
2. N.Ž. Šekuljica et al., Decolorization of anthraquinonic dyes from textile effluent using horseradish peroxidase: optimization and kinetic study. *Sci. World J.* **2015**, 1–12 (2015)
3. A. Gürses et al., Dyes and pigments: their structure and properties, *Dyes and Pigments* (Springer, New York, 2016), pp. 13–29
4. M. Ramya et al., A facile and efficient single step ball milling process for synthesis of partially amorphous Mg–Zn–Ca alloy powders for dye degradation. *J. Alloy. Compd.* **696**, 185–192 (2017)
5. K.-T. Chung, Azo dyes and human health: a review. *J. Environ. Sci. Health C* **34**(4), 233–261 (2016)
6. R. Hasegawa, *Glassy Metals: Magnetic, Chemical and Structural Properties* (CRC Press, Boca Raton, 2018)

7. H. Li, Y. Zheng, Recent advances in bulk metallic glasses for biomedical applications. *Acta Biomater.* **36**, 1–20 (2016)
8. T. Qi et al., Soft magnetic Fe<sub>25</sub>Co<sub>25</sub>Ni<sub>25</sub>(B, Si)<sub>25</sub> high entropy bulk metallic glasses. *Intermetallics* **66**, 8–12 (2015)
9. K. Sarlar, I. Kucuk, Thermal and magnetic characterisation of (Co<sub>0.402</sub>Fe<sub>0.201</sub>Ni<sub>0.067</sub>B<sub>0.227</sub>Si<sub>0.053</sub>Nb<sub>0.05</sub>)<sub>100-x</sub>Cu<sub>x</sub> bulk metallic glasses. *Philosophical Mag.* **97**(7), 489–496 (2017)
10. S. Hu et al., Tandem laser ablation synthesis in solution-galvanic replacement reaction (LASiS-GRR) for the production of PtCo nanoalloys as oxygen reduction electrocatalysts. *J. Pow. Sources* **306**, 413–423 (2016)
11. S.J. Hwang et al., Ternary Pt–Fe–Co alloy electrocatalysts prepared by electrodeposition: elucidating the roles of Fe and Co in the oxygen reduction reaction. *J. Phys. Chem. C* **115**, 2483–2488 (2011)
12. S. Zhai et al., Effects of pre-compression on the microstructure, mechanical properties and corrosion resistance of Cu<sub>47.5</sub>Zr<sub>47.5</sub>Al<sub>5</sub> bulk metallic glasses. *J Non-Cryst. Solids* **481**, 383–390 (2018)
13. Z. Guo et al., Highly stable and active PtNiFe dandelion-like alloys for methanol electrooxidation. *J. Mater. Chem. A* **1**, 13252–13260 (2013)
14. S.-W. Chou et al., Surfactant-directed synthesis of ternary nanostructures: nanocubes, polyhedrons, octahedrons, and nanowires of PtNiFe. Their shape-dependent oxygen reduction activity. *Chem. Mater.* **24**, 2527–2533 (2012)
15. S. Hu et al., A facile and surfactant-free route for nanomanufacturing of tailored ternary nanoalloys as superior oxygen reduction reaction electrocatalysts. *Catal. Sci. Technol.* **7**, 2074 (2017)
16. Y.G. Yao et al., Carbothermal shock synthesis of high-entropy-alloy nanoparticles. *Science* **359**, 1489–1494 (2018)
17. H. Eskalen et al., Amorphous alloys, degradation performance of Azo dyes. *arXiv preprint arXiv:1709.06941* (2017)
18. X. Wang et al., Efficient degradation of rhodamine B using Fe-based metallic glass catalyst by Fenton-like process. *Chemosphere* **117**, 638–643 (2014)
19. J.Q. Wang et al., Rapid degradation of Azo dye by Fe-based metallic glass powder. *Adv. Funct. Mater.* **22**(12), 2567–2570 (2012)
20. X. Qin et al., Mechanism and kinetics of treatment of acid orange II by aged Fe–Si–B metallic glass powders. *J. Mater. Sci. Technol.* **33**(10), 1147–1152 (2017)
21. P. Liu et al., Synthesis of an Fe rich amorphous structure with a catalytic effect to rapidly decolorize Azo dye at room temperature. *ACS Appl. Mater. Interfaces* **6**(8), 5500–5505 (2014)
22. S. Liang et al., Rapid malachite green degradation using Fe<sub>73.5</sub>Si<sub>13.5</sub>B<sub>9</sub>Cu<sub>1</sub>Nb<sub>3</sub> metallic glass for activation of persulfate under UV–Vis light. *Mater. Des.* **119**, 244–253 (2017)
23. Z. Jia et al., Heterogeneous photo Fenton-like degradation of cibacron brilliant red 3B-A dye using amorphous Fe<sub>78</sub>Si<sub>9</sub>B<sub>13</sub> and Fe<sub>73.5</sub>Si<sub>13.5</sub>B<sub>9</sub>Cu<sub>1</sub>Nb<sub>3</sub> alloys: the influence of adsorption. *J. Taiwan Inst. Chem. Eng.* **71**, 128–136 (2017)
24. Z. Jia et al., Surface aging behaviour of Fe-based amorphous alloys as catalysts during heterogeneous photo Fenton-like process for water treatment. *Appl. Catal. B* **204**, 537–547 (2017)
25. Z. Jia et al., Ultra-sustainable Fe<sub>78</sub>Si<sub>9</sub>B<sub>13</sub> metallic glass as a catalyst for activation of persulfate on methylene blue degradation under UV–Vis light. *Sci. Rep.* **6**, 38520 (2016)
26. Z. Deng et al., Fe-based metallic glass catalyst with nanoporous surface for azo dye degradation. *Chemosphere* **174**, 76–81 (2017)
27. S. Das et al., Synergistic catalytic effect of iron metallic glass particles in direct blue dye degradation. *J. Mater. Res.* **30**(8), 1121–1127 (2015)
28. Y. Zhao et al., Synthesis of Mg–Zn–Ca metallic glasses by gas-atomization and their excellent capability in degrading azo dyes. *Mater. Sci. Eng. B* **181**, 46–55 (2014)
29. C. Kursun, M. Gogebakan, H. Eskalen, Mechanical properties, microstructural and thermal evolution of Mg<sub>65</sub>Ni<sub>20</sub>Y<sub>15-x</sub>Si<sub>x</sub> (X = 1, 2, 3) alloys by mechanical alloying. *Mater. Res. Express* **5**, 036512 (2018)
30. Q.-Q. Jin, C.-F. Fang, S.-B. Mi, Formation of long-period stacking ordered structures in Mg<sub>88</sub>M<sub>5</sub>Y<sub>7</sub> (M=Ti, Ni and Pb) casting alloys. *J. Alloy. Compd.* **568**, 21–25 (2013)
31. M. Jiang et al., Phase equilibria of the long-period stacking ordered phase in the Mg–Ni–Y system. *Intermetallics* **57**, 127–132 (2015)
32. J. Liu et al., Facilitating de/hydrogenation by long-period stacking ordered structure in Mg based alloys. *Int. J. Hydrog. Eng.* **38**(25), 10438–10445 (2013)
33. C. Kursun et al., Mg<sub>65</sub>Ni<sub>20</sub>Y<sub>15-x</sub>Ag<sub>x</sub> (X = 1, 2, 3, 5) alloys prepared via atmosphere controlled induction system. *Can. J. Phys.* **96**(7), 810–815 (2018)
34. C. Kursun, M. Gogebakan, Characterization of nanostructured Mg–Cu–Ni powders prepared by mechanical alloying. *J. Alloy Compd.* **619**, 138–144 (2015)
35. T. Varol, A. Canakci, The effect of type and ratio of reinforcement on the synthesis and characterization Cu-based nanocomposites by flake powder metallurgy. *J. Alloy Compd.* **649**, 1066–1074 (2015)
36. F. Yilmaz et al., Fabrication of cobalt nano-particles by pulsed wire evaporation method in nitrogen atmosphere. *Powder Technol.* **235**, 1047–1052 (2013)
37. Y. Zhu, G. Zheng, Z. Dai, J. Mu, Z. Yao, Mono-disperse SrMoO<sub>4</sub> nanocrystals: synthesis, luminescence and photocatalysis. *J. Mater. Sci. Technol.* **33**, 834–842 (2017)
38. Z. Jia et al., Surface aging behaviour of Fe-based amorphous alloys as catalysts during heterogeneous photo Fenton-like process for water treatment. *Appl. Catal. B* **204**, 537–547 (2017)
39. X. Chen et al., Preparation of ZnO photocatalyst for the efficient and rapid photocatalytic degradation of Azo dyes. *Nanoscale Res. Lett.* **12**, 143–153 (2017)
40. D. Hazarika, N. Karak, Photocatalytic degradation of organic contaminants under solar light using carbon dot/titanium dioxide nanohybrid, obtained through a facile approach. *Appl. Surf. Sci.* **376**, 276–285 (2016)

**Publisher's Note** Springer Nature remains neutral with regard to jurisdictional claims in published maps and institutional affiliations.